

Satellite interferometry for mapping surface deformation time series in one, two and three dimensions: A new method illustrated on a slow-moving landslide



Sergey Samsonov^{a,*}, Antoine Dille^{b,c}, Olivier Dewitte^b, François Kervyn^b, Nicolas d'Oreye^{d,e}

^a Natural Resources Canada, 560 Rochester Street, Ottawa, ON K1A0E4, Canada

^b Department of Earth Sciences, Royal Museum for Central Africa, Leuvensesteenweg 13, 3080 Tervuren, Belgium

^c Department of Geography, Earth System Science, Vrije Universiteit Brussel, Pleinlaan 2, 1050 Brussels, Belgium

^d European Center for Geodynamics and Seismology, Rue Josy Welter 19, L-7256 Walferdange, Luxembourg

^e National Museum of Natural History, Department Geophysics/Astrophysics, Rue Josy Welter 19, L-7256 Walferdange, Luxembourg

ARTICLE INFO

Keywords:

DInSAR
3D surface deformation time series
Multidimensional small baseline subset (MSBAS)
Surface parallel motion
Landslide
Tropical environment

ABSTRACT

Space-borne Differential Interferometric Synthetic Aperture Radar (DInSAR) has been extensively used in the last two decades to measure ground surface deformation, providing key information for the characterization and understanding of many natural and anthropogenic processes. However, conventional DInSAR technique measures only one component of the surface deformation (i.e. the satellite's line-of-sight (LOS)), causing the interpretation of DInSAR measurements to be challenging and potentially narrowing the understanding of the mechanisms and dynamics of the deformation processes at work. Presently available methods that estimate 3D surface deformation from DInSAR generally operate on individual interferograms and therefore do not produce 3D surface deformation time series. However, the availability of time series is essential for studying surface deformation processes, bringing information on, e.g., temporally and spatially-variable external forcing conditions and characteristics of future deformation patterns. The Multidimensional Small Baseline Subset (MSBAS) method was already able to produce 2D (east and vertical) surface deformation time series from multi-tracks and multi-sensors DInSAR data. Here we propose a novel version of the MSBAS (MSBAS-3D) method that can produce 3D (north, east, and vertical) surface deformation time series from ascending and descending DInSAR data. This new method proposes measuring the surface deformation for processes producing motion parallel to the surface, such as landslides and glacier flows, while conserving the DInSAR accuracy. The ability of MSBAS-3D to capture the full 3D deformation pattern of processes with a surface signature is illustrated for a large, slow-moving, deep-seated landslide, for which long DInSAR and dGNSS time series, as well as ground truth data, are available. Surface deformation is measured over a four-year period using 1D (LOS), 2D and 3D MSBAS methods, and the advantages and limitations of each approach are described. In this case, the novel MSBAS-3D technique produces superior results that greatly simplify interpretation of the processes at work. The MSBAS-3D software can be downloaded from <http://insar.ca/>.

1. Introduction

Surface deformation information is a key parameter for characterization of natural and anthropogenic processes such as earthquakes, volcanic eruptions, landslides, glacier flows, and subsidence and uplift due to resource exploitation (e.g. Colesanti and Wasowski, 2006; Wasowski and Bovenga, 2014; Elliott et al., 2016; Bayer et al., 2017; Dong et al., 2018; Li et al., 2019). To this end, space-borne Differential Interferometric Synthetic Aperture Radar (DInSAR) allows the

derivation of surface deformation with wide spatial coverage, millimetre precision, high temporal and spatial resolutions and all-day and all-weather working capabilities (Massonnet and Feigl, 1998; Rosen et al., 2000).

However, conventional DInSAR technique measures only one component of the surface deformation - in the satellite's line-of-sight (LOS) (Wright et al., 2004; Hu et al., 2014). This makes interpretation of DInSAR measurements challenging and narrows the understanding of the mechanisms and dynamics of the deformation processes at work.

* Corresponding author.

E-mail address: sergey.samsonov@canada.ca (S. Samsonov).

Different methods were therefore developed to provide direct measurements of the two (2D, east and vertical) (e.g. Samsonov and d'Oreye, 2012, 2017) or the three (3D, north, east and vertical) components of surface deformation at one point in time (e.g. Wright et al., 2004; Gourmelen et al., 2011; Ng et al., 2012; Raucooles et al., 2013; Shi et al., 2018). The most straightforward strategy for deriving 3D surface deformation is to combine multiple DInSAR LOS measurements with different viewing geometries. However, trying to derive 3D deformation from multi-orbit satellite SAR observations alone poorly constrains the north component of motion (Fuhrmann and Garthwaite, 2019). Indeed, due to the small inter-satellite variation in SAR satellite orbits (i.e. near-polar orbit), this approach may be applied solely for a very specific case - in high latitude areas where the azimuth angle diversity is higher (e.g. Gray, 2011; Hu et al., 2014). Larger diversity in acquisition geometry can be obtained using airborne DInSAR, that allows acquisition with any desired azimuthal direction (e.g. Delbridge et al., 2016; Handwerger et al., 2019). However, the cost of such acquisitions limits the temporal sampling. As a result of these difficulties, the retrieval of 3D surface deformation therefore commonly consists of merging conventional DInSAR LOS measurements with other types of measurements, that may rely either on SAR imagery or ancillary data, such as GNSS measurements (e.g. Samsonov and Tiampo, 2006; Samsonov et al., 2007, 2008; Hu et al., 2014).

East and vertical deformation components are often derived from conventional DInSAR applied to two (or more) different satellite tracks, that are then combined with outputs from either speckle tracking (Wright et al., 2004; De Michele et al., 2010; Raucooles et al., 2013; Shi et al., 2018) or Multiple Aperture Interferometry (MAI) (e.g. Gourmelen et al., 2011) to retrieve the north component of deformation (Hu et al., 2014). With the speckle tracking technique, range and azimuth deformation are calculated from the offset of a given point on the ground using local correlation analysis between two images (Michel et al., 1999; Leprince et al., 2007). This method is applied to either the amplitude (Michel et al., 1999; Pathier et al., 2006) or the phase information (Gray et al., 2001; Pattyn and Derauw, 2002) of the SAR images. While it is not affected by signal saturation with high deformation gradient, speckle tracking precision is much lower, with values between 1/30th to 1/10th of the image pixel size, than the millimetre-scale precision that can be achieved with DInSAR (Leprince et al., 2007; Raucooles et al., 2013; Hu et al., 2014). This implies that the use of the speckle tracking technique is often limited to the case of relatively large deformation. The other method, MAI, aims at extending the applicability of DInSAR to along-track deformation based on split-beam DInSAR processing (Bechor and Zebker, 2006; Jung et al., 2009; Gourmelen et al., 2011). Bechor and Zebker (2006) found that for interferograms with coherence of 0.4 and higher, MAI outperforms speckle tracking analysis in precision. However, such high coherence is relatively uncommon, particularly in vegetated regions. Pepe et al. (2016); Pepe and Calo (2017) proposed to derive 3D deformation from ascending and descending data by applying higher order regularizations; this technique was used for mapping 3D deformation time series at the Big Island of Hawaii.

Another strategy used to overcome the constraint originating from the geometry of SAR observation is to make assumptions about deformation processes being studied (Hu et al., 2014). In the case of landslides and glacier flows, a reasonable assumption is that motion occurs parallel to the surface, although not necessarily downslope. By reducing the degrees of freedom from three to two, with this assumption one may resolve the three components of motion from (at least) one ascending and one descending DInSAR datasets. This approach has

been demonstrated on glaciers in polar regions using single or few ascending and descending interferograms from the ERS-1/2 tandem mission (e.g. Joughin et al., 1998; Mohr et al., 1998; Gourmelen et al., 2011; Kumar et al., 2011). Notti et al. (2014); Kalia (2018); Hu et al. (2018, 2019) applied a similar principle on landslides, here projecting measured LOS velocity along the steepest downslope (one step further from assuming a movement parallel to the surface) to obtain estimates of the landslide motion. Assumption of motion along the steepest downslope may however be seen as too strict, as it does not allow consideration of lateral motion.

Time series are essential for studying surface deformation processes, which ideally calls for an integrated multi-sensor, multi-track and multi-temporal DInSAR measurements approach (Hu et al., 2013, 2014). However, all the previous methods discussed above, derived 3D surface deformation from either individual interferograms, or separate or interpolated ascending and descending datasets. Because of the mismatch in the acquisition times of ascending and descending datasets, these methods cannot be used to merge all available DInSAR data for producing a single set of temporally dense, 3D surface deformation time series (Samsonov and d'Oreye, 2012).

Here, we propose a novel version of the Multidimensional Small Baseline Subset (MSBAS) method (Samsonov and d'Oreye, 2012, 2017), MSBAS-3D, that is able to produce 3D (north, east, and vertical) surface deformation time series from multi-track and multi-sensor DInSAR data. This new method aims at measuring surface deformation for processes involving motion parallel to the surface, such as landslides and glacier flows. The ability of MSBAS-3D to capture the full 3D deformation pattern and the benefits for the understanding of the processes at work are illustrated for a large, slow-moving, deep-seated landslide for which long DInSAR and dGNSS time series, as well as ground truth data, are available.

2. Methodology

The Multidimensional Small Baseline Subset (MSBAS) methodology is developed for simultaneous post processing of the hundreds to thousands of individual interferograms produced by a conventional DInSAR processing (Samsonov and d'Oreye, 2012, 2017). Depending on the number of datasets, their acquisition parameters and specified control flags, the technique produces line-of-sight (MSBAS-1D), east and vertical (MSBAS-2D), and now north, east, and vertical (MSBAS-3D) surface deformation time series. The output of processing consists of cumulative time series for each acquisition epoch and linear deformation rate for each pixel that remains coherent throughout the entire time span. A brief derivation of all three techniques is provided below, with an emphasis on the new MSBAS-3D technique.

2.1. MSBAS-1D

In case of a single DInSAR dataset computed from data acquired by a sensor with an azimuth angle θ and an incidence angle ϕ , the LOS surface deformation time series is computed by applying the Small Baseline Subset (SBAS) technique (Berardino et al., 2002; Usai, 2003). The SBAS technique implemented in MSBAS-1D software is called when one or more DInSAR datasets with similar incidence and azimuth angles are provided. In matrix form MSBAS-1D can be written as

$$AV_{los} = \Phi, \quad V_{los} = A^+ \Phi, \quad d_{los}^{i+1} = d_{los}^i + V_{los}^i \Delta t^i \quad (1)$$

where A is a matrix constructed from the time intervals between

consecutive SAR acquisitions, V_{los} is a vector of the unknown LOS deformation velocities, Φ is a vector of observed DInSAR values, A^+ is a pseudo-inverse of matrix A found by applying the Singular Value Decomposition (SVD), and d_{los}^i is a cumulative LOS deformation at the time t^i .

The LOS deformation velocity V_{los} is related to the three components of the deformation velocity vector V with components V_N , V_E , V_V through the following equation

$$V_{los} = \mathbf{S}V = S_N V_N + S_E V_E + S_V V_V \quad (2)$$

where $\mathbf{S} = \{S_N, S_E, S_V\} = \{\sin\theta \sin \phi, -\cos \theta \sin \phi, \cos \phi\}$ is a LOS unit vector with north, east and vertical components S_N , S_E , S_V .

2.2. MSBAS-2D

When both, ascending and descending DInSAR datasets acquired over the same area and time period are available, the MSBAS-2D technique computes east and vertical components of surface deformation time series. This solution is approximate because the contribution of the third, north component is neglected for the reason that $S_N < S_E, v$ and $V_N \approx V_E, v$. In matrix form MSBAS-2D can be written as

$$\begin{pmatrix} \widehat{A} \\ \lambda L \end{pmatrix} \begin{pmatrix} V_E \\ V_V \end{pmatrix} = \begin{pmatrix} \widehat{\Phi} \\ 0 \end{pmatrix}, \quad \begin{pmatrix} V_E \\ V_V \end{pmatrix} = \begin{pmatrix} \widehat{A} \\ \lambda L \end{pmatrix}^+ \begin{pmatrix} \widehat{\Phi} \\ 0 \end{pmatrix}, \quad d_{E,U}^{i+1} = d_{E,U}^i + V_{E,U}^i \Delta t^i \quad (3)$$

where the matrix $\widehat{A} = \{s_E A, s_V A\}$ consists of the matrix A (described above) multiplied by the east and vertical components of the LOS unit vector \mathbf{S} .

The Tikhonov regularization matrix L multiplied by the regularization parameter λ is used for regularizing time series (Tikhonov and Arsenin, 1977). The effect of regularization is similar to applying a low-pass filter and it is recommended when the acquisition times of ascending and descending datasets do not match. The matrix A , as well as the regularization matrices L of zeroth, first and second orders were explicitly derived in (Samsonov, 2010; Samsonov and d'Oreye, 2017). As in the previous case, the unknown east and vertical components of deformation velocities V_E and V_V for each acquisition epoch and pixel are solved by applying SVD and the 2D surface deformation time series are reconstructed from computed deformation velocities by the numerical integration.

2.3. MSBAS-3D

In certain cases, the contribution of the north-south component of displacement is too large to be neglected ($S_N < S_E, v$, $V_N \approx V_E$, and $V_N > V_V$). By assuming that the motion occurs parallel to the surface, we can however reduce the degrees of freedom from three to two, allowing resolving all three components of motion from (at least) one ascending and one descending DInSAR datasets. This assumption is for instance suited for characterizing gravity-driven processes such as landslides and glacier flows. The constraint can be written in terms of deformation velocities in the following form

$$V_V = \frac{\partial H}{\partial X_N} V_N + \frac{\partial H}{\partial X_E} V_E \quad (4)$$

where H is the topographic height and $\frac{\partial H}{\partial X_N}$ and $\frac{\partial H}{\partial X_E}$ are first derivatives in the north X_N and east X_E directions. The $\frac{\partial H}{\partial X_N}$ and $\frac{\partial H}{\partial X_E}$ values can be computed from DEM using, for example, the Generic Mapping Tools (GMT) *grdmath -M DDY/DDX* command. Prior low-pass filtering of DEM (e.g. using GMT *grdfilter* command) is recommended for reducing

sensitivity to surface features that do not affect the ground motion originated at some (shallow) depth. It is likely that sliding surface at depth is smoother than DEM. The magnitude of a low-pass filter needs to be sufficiently strong so the resulting surface has a slope equal to an overall slope of the form that host the landslide.

The MSBAS-3D technique that computes constrained 3D surface deformation time series can be written in matrix form as

$$\begin{pmatrix} \widehat{A} \\ H \\ \lambda L \end{pmatrix} \begin{pmatrix} V_N \\ V_E \\ V_V \end{pmatrix} = \begin{pmatrix} \widehat{\Phi} \\ 0 \\ 0 \end{pmatrix}, \quad \begin{pmatrix} V_N \\ V_E \\ V_V \end{pmatrix} = \begin{pmatrix} \widehat{A} \\ H \\ \lambda L \end{pmatrix}^+ \begin{pmatrix} \widehat{\Phi} \\ 0 \\ 0 \end{pmatrix}, \quad d_{N,E,V}^{i+1} = d_{N,E,V}^i + V_{N,E,V}^i \Delta t^i \quad (5)$$

where the matrix $\widehat{A} = \{s_N A, s_E A, s_V A\}$ consists of the matrix A (described above) multiplied by the north, east and vertical components of the LOS unit vector \mathbf{S} . The matrix $H = \left\{ \frac{\partial H}{\partial X_N}, \frac{\partial H}{\partial X_E}, -1 \right\}$ represents the motion parallel to the surface constraint. The unknown north, east and vertical components of deformation velocities V_N , V_E and V_V for each acquisition epoch and pixel are solved by applying SVD and the surface deformation time series are reconstructed from the computed deformation velocities by the numerical integration.

For some combinations of acquisition parameters and topographic gradients, (5) may become ill-conditioned, which can be assessed by computing condition number for all possible topographic gradients for given acquisition parameters.

2.4. Computational aspects

Matrices in Eqs. (1), (3), and (5) typically have hundreds of columns and thousands of rows, corresponding to the total number of SAR images and DInSAR interferograms, respectively. Computation of the Singular Value Decomposition (SVD) of such large matrices is intensive. In case of the 1D analysis, viewing geometry \mathbf{S} is irrelevant so SVD computation is performed only once. In case of the 2D analysis, constant viewing geometry \mathbf{S} is assumed. This allows performing SVD computation only once, which results in a slight reduction of precision. In case of the 3D deformation analysis, SVD inversion is performed for each coherent pixel in order to account for the spatially varying constraint so varying viewing geometry is implemented as well. The typical processing time of MSBAS-1D and MSBAS-2D is only a few tens of minutes, while the typical processing time of MSBAS-3D can reach several hours (for a typical grid of a few thousand pixels in each dimension) due to the large number of SVD computations required.

Unlike other advanced methods such as StaMPS (Hooper, 2008), MSBAS processing is incremental. The addition of new SAR images requires computing of only the few interferograms satisfying user-defined baseline criteria before executing MSBAS processing.

3. Test case and data

The ability to unravel surface deformation pattern using the different level of processing of the MSBAS method is illustrated on a large landslide, for which long DInSAR and dGNSS time series, as well as ground truth data, are available (Nobile et al., 2018).

3.1. Funu landslide

Funu landslide (2°31'S, 28°50'E, Fig. 1) is located in the densely populated City of Bukavu, situated in the Kivu Rift (western branch of the East African Rift System) in eastern Democratic Republic of the

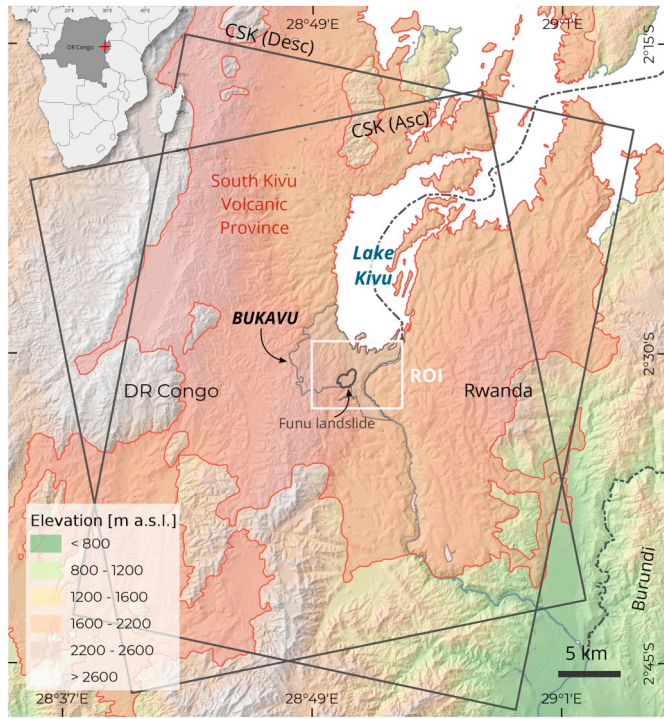


Fig. 1. Funu landslide is located in the city of Bukavu, eastern DR Congo. It lies within the South Kivu Volcanic Province that is formed of sequences of late Miocene to Pleistocene sub-horizontal basaltic lava layers. Outlined in white is shown the area processed with MSBAS. The footprints of the ascending and descending COSMO-SkyMed SAR images used in this study are outlined in black.

Congo. This region is characterised by a high susceptibility to landslides due to a combination of natural predisposing and triggering factors (e.g., high rainfall intensities, moderate to high seismicity, deep weathering and steep landscapes) (Jacobs et al., 2016; Monsieurs et al., 2018; Depicker et al., 2019; Dille et al., 2019). Located in the tropics, the region is affected by persistent cloud cover over most of the year, making DInSAR a key remote sensing tool for the study of landslides in this area (Nobile et al., 2018).

This 1.5 km^2 slow-moving slope instability was formed thousands of years ago (Moeyersons et al., 2004). The depth of this bedrock landslide can be estimated to be of at least 100 m, i.e. the average height of its main scarp (Dewitte and Demoulin, 2005; Larsen et al., 2010). The landslide developed in sequences of late Miocene to Pleistocene sub-horizontal basaltic lava layers (Fig. 2b) that make up the South Kivu Volcanic Province (Fig. 1). An accurate delineation of the layers does not exist. However, the presence of springs at different elevations shows that their permeability varies, attesting to perched water tables. Weathering of some layers can be very intense with a regolith thickness that can be more than 10 m (Fig. 2c). The distribution of the weathering is highly uneven, sometimes having important changes over short distances of a few tens of meters (Moeyersons et al., 2004). The landslide is currently prone to surface deformation as attested to by continuous damage to infrastructure and buildings (Moeyersons et al., 2004; Balegamire et al., 2017). This landslide is also densely populated, with approximately 80 thousand people living directly on it (Michellier et al., 2016).

Nobile et al. (2018) provided a first analysis of the Funu landslides

kinematics and mechanisms by combining one year of DInSAR measurements from 70 Cosmo-SkyMed SAR images acquired between 21 March 2015 and 19 April 2016, processed using the StaMPS SBAS approach (Lanari et al., 2007; Hooper, 2008) and on-site dGNSS measurements. They measured deformation of up to 70 mm/yr in the ascending and descending LOS directions. These measurements were in good agreement with dGNSS, except for one zone of the landslide that corresponds to a recent, smaller subsequent landslide. There, dGNSS measurements showed deformation an order of magnitude larger than DInSAR (up to 500 mm/yr while converted to LOS). The limit in the maximum detectable deformation resolvable by the X-band DInSAR was reached (Nobile et al., 2018). The study by Nobile et al. (2018) confirmed that the Funu landslide is mostly driven by a rotational mechanism with a prominent main scarp and a characteristic back-tilted bench. Several minor scarps, probably linked to secondary shear surfaces, are present in the zone of depletion and delimit individual blocks. From rotational in the depletion zone, the main movement develops a more planar behaviour with flow-like features in its runout and accumulation zones (as suggested from its morphometry). They concluded that the dense urban fabric, the relatively low velocity of the ground deformation, and the general eastward topography with the average slope of about 6.5 degrees (vs 45 degree SAR incidence angle) that avoids shadowing and foreshortening effects make the Funu landslide a particularly interesting site for DInSAR analysis.

3.2. COSMO-SkyMed images

We used 176 ascending and 166 descending COSMO-SkyMed images that were acquired between 24 March 2015 and 3 January 2019 (Table 1). Ascending images were acquired with the incidence angle of 41 degrees, range pixel spacing of 1.3 m and azimuth pixel spacing of 2.3 m. Descending images were acquired with the incidence angle of 50 degrees, range pixel spacing of 1.7 m and azimuth pixel spacing of 2.1 m.

Each COSMO-SkyMed set was processed independently with the GAMMA software (Wegmüller and Werner, 1997). Ascending image acquired on 5 February 2017 and descending image acquired on 5 May 2017 were selected as masters for respective sets and remaining images were re-sampled into the master geometry. Multi-looking factor of 2 in range and azimuth were used, as well as a maximal perpendicular baselines of 600 m (Fig. 3). The topographic phase was removed using the 1 arc-second ($\sim 30 \text{ m}$) resolution Shuttle Radar Topography Mission Digital Elevation Model (SRTM DEM, Fig. 1). Differential interferograms were filtered using the adaptive filter with a filtering function based on local fringe spectrum (Goldstein and Werner, 1998) and unwrapped using the minimum cost flow algorithm (Costantini, 1998). The residual orbital ramp was corrected by applying baseline refinement algorithm implemented in the GAMMA software that utilizes unwrapped phase and topographic height at selected coherent pixels to solve for a refined baseline. Minor interpolation of each interferogram was performed in order to improve the spatial coverage reduced by decorrelation. Then, ascending and descending interferograms were geocoded and resampled using the Geospatial Data Abstraction Library (GDAL) program to a common lat/lon grid with a uniform spatial sampling of 5 m.

Geocoded to a common grid, ascending and descending interferograms with an average coherence after filtering above 0.5 were processed with the MSBAS techniques to produce deformation time series and annual linear deformation rates over Funu landslide and its close surroundings.

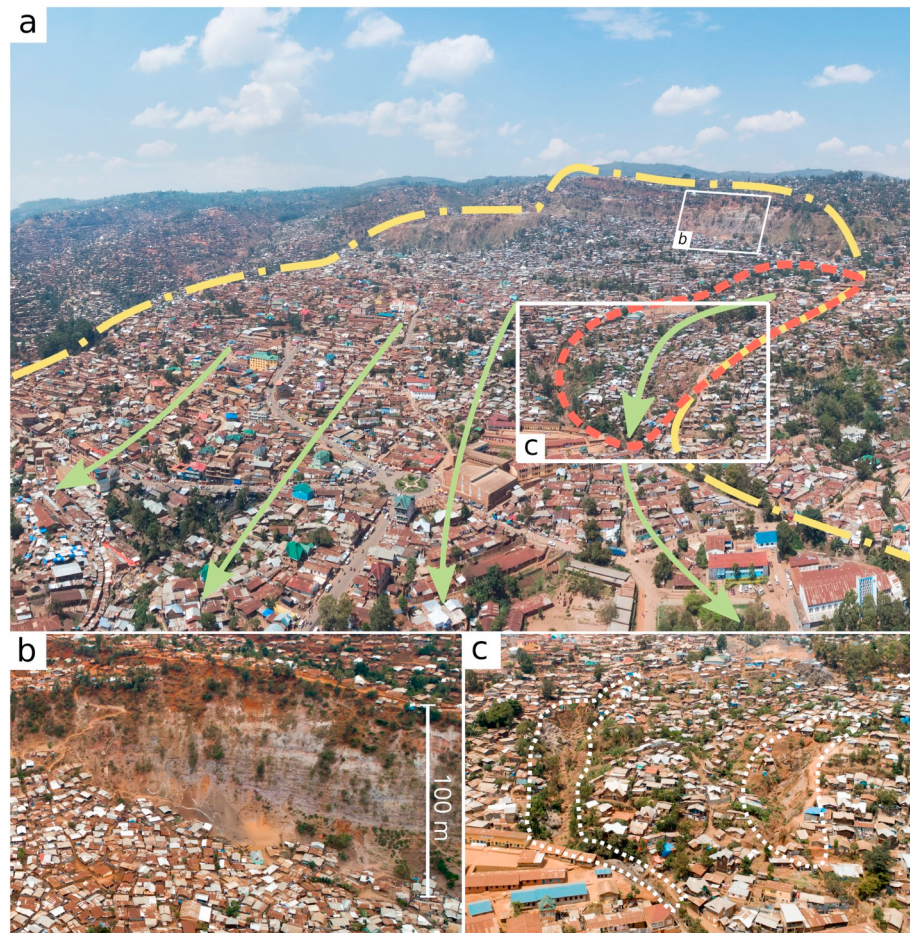


Fig. 2. Drone photographs of Funu landslide acquired in September 2018. a) General view of the landslide, with its extent outlined in yellow and green arrows indicating principal direction of movement. The fastest moving region, where discrepancies between DInSAR and dGNSS are observed, is outlined in red. Note constraints from topography and apparent divergent motion at landslides bottom. The total landslide height is about 400 m while the height of the main scarp is up to 100 m. b) Sequences of late Miocene to Pleistocene sub-horizontal basaltic lava layers apparent over the main scarp. c) Gullies delineating the toe of the fastest landslide unit. Their presence highlights the deep weathering of some basaltic layers, with a regolith thickness that can easily exceed 10 m. (For interpretation of the references to colour in this figure legend, the reader is referred to the web version of this article.)

Table 1

COSMO-SkyMed SAR data used in this study, θ is azimuth angle and ϕ is incidence angle, N is number of SLC images and M is number of DInSAR interferograms computed for each data set. 2D and 3D time series span 24 March 2015–3 January 2019 interval when both ascending and descending data are available.

DInSAR data set	θ	ϕ	Temporal coverage	N	M
COSMO-SkyMed (asc)	-12	41	20,150,324–20,190,103	176	963
COSMO-SkyMed (dsc)	-168	50	20,150,324–20,190,103	166	924
Total			20,150,324–20,190,103	342	1887

3.3. dGNSS measurements

The DInSAR-derived deformation rates are validated through a comparison with the dGNSS measurements acquired by repeated measurement campaigns. The dGNSS measurements were captured in a static acquisition mode with Leica GX1230 dual-frequency receivers and post-processed with Leica Geosystems post-processing software. The dGNSS measurements were acquired over already in place benchmarks that are solid concrete structures, such as a water fountains, concrete sewers or street curbs. Measurement duration (5 min) at roving sites was constrained by the safety of operators and equipment in this area, although position accuracy would have benefited from longer sessions. The accuracy achieved for the dGNSS locations was

estimated as 7.5 mm for the horizontal and 16.5 mm for the vertical components. These uncertainties refer to the internal precision of the measurement, field conditions, and data post-processing. It was also assumed that all benchmarks and the reference station move at the same rift opening rate of about 2 mm/year (Delvaux et al., 2017).

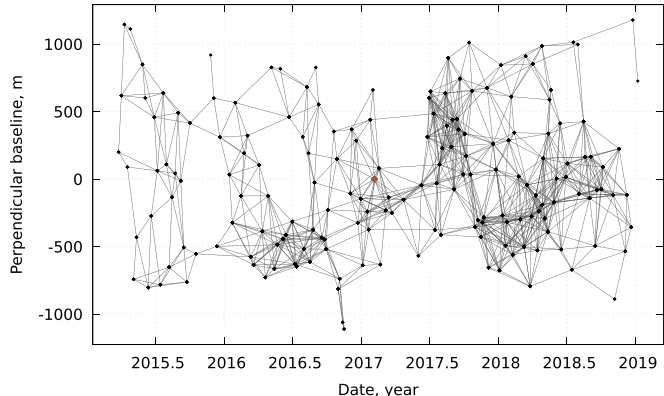
3.4. DEM derivatives

The $\frac{\partial H}{\partial X_N}$ and $\frac{\partial H}{\partial X_E}$ values (Fig. 4) were computed from SRTM DEM using the Generic Mapping Tools (GMT) *grdmath -M DDY/DDX* command. Prior low-pass filtering of DEM was applied using GMT *grdfilter* command to computed average values in 65 m window and therefore removing surface features that are not expected to affect the ground motion at depth.

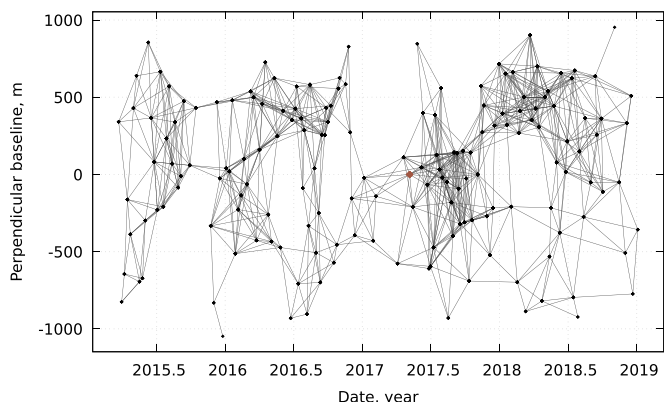
4. Results

Figs. 5–7 show annual linear deformation rates for the city of Bujumbura computed with the 1D, 2D, and 3D MSBAS techniques. For all methods, the deformation signal of the large Funu landslide clearly stands out.

The 1D ascending and descending linear deformation rates computed with (1) show distance to satellite (line-of-sight) displacements. Absolute maximal rates of displacement are similar (0.05 m/year)



(a) Ascending



(b) Descending

Fig. 3. Spatial and temporal baselines of COSMO-SkyMed ascending and descending interferograms used in this study. Brown points mark ascending and descending master images. (For interpretation of the references to colour in this figure legend, the reader is referred to the web version of this article.)

between ascending (Fig. 5(a)) and descending (Fig. 5(b)) datasets, but the extent of the deformation measured over the Funu landslide in the descending map is significantly lesser than in the ascending map.

The 2D east and vertical linear deformation rates computed with (3) show eastward motion with a maximum magnitude of 0.05 m/year

(Fig. 6(a)) and downward motion with a magnitude up to 0.02 m/year (Fig. 6(b)). Only the signal of the landslide is shown in the eastward component deformation map, while the vertical displacement map highlights also other deforming regions within the city.

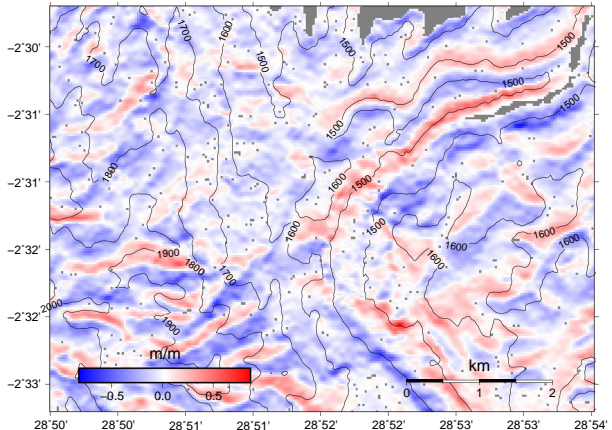
The 3D north, east and vertical linear deformation rates computed with (5) are shown in Fig. 7. The north deformation rate map (Fig. 7(a)) highlights areas with both northern and southern motion with a maximum rate of 0.02 m/year over different places within the city. The east map (Fig. 7(b)) shows eastward deformation with a maximum rate of 0.05 m/year that is nearly identical to the 2D case (Fig. 6(a)) and is dominated by the signal of the large Funu landslide. The vertical map (Fig. 7(c)) highlights only downward motion with a maximum rate of 0.02 m/year. Similarly as with the 2D case (Fig. 6(a)), signals of other deforming regions are captured within the city. The overall scale of the deformation measured with the 3D case is however of lower magnitude.

Annual horizontal displacements measured with MSBAS-3D method are plotted as vectors in Fig. 8, along with the dGNSS deformation vectors. It clearly highlights an advancing landslide lobal front, as well effect of lateral constraints from the surrounding non-moving topography. The directions of movement measured by dGNSS and DInSAR are in general in good agreement at F14, F15, F17, F18 and F20 dGNSS sites, for which the coefficient of determination R^2 is greater than 0.75 for north and east deformation components.

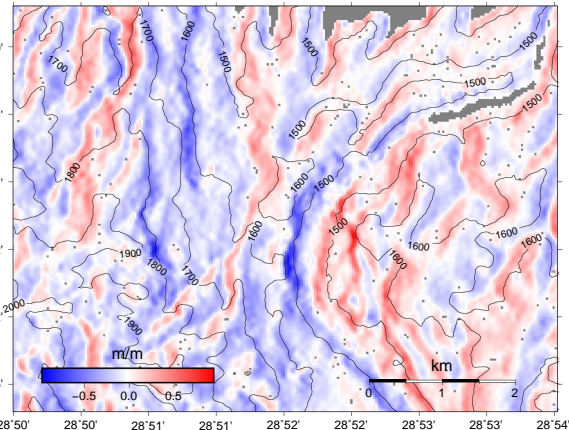
The 3D surface deformation time series for points P1-P6 (marked in Fig. 7) that approximately correspond to regions of fastest motion within the landslide are shown in Fig. 9. Standard deviation, computed in 5×5 pixels ($\sim 25 \times 25$ m) window, measures deviation from a mean value rather than precision of the measurement technique because deformation signal and measurement noise cannot be separated. Standard deviation over a larger 33×33 pixels ($\sim 165 \times 165$ m) window at a region that does not experience observable ground deformation allows measuring precision of this measurement technique. The estimated precision is better than 2.8, 1.4, and 0.5 mm for north, east and vertical components respectively.

Deformation produced by the Funu landslide clearly stands out in all deformation maps. Discrimination between vertical and horizontal movements provided by MSBAS-2D and MSBAS-3D (Figs. 6 and 7) show that, overall, Funu landslide movement is mostly horizontal (to the east). Half-moon deformation patterns highlight rotational movements at the head of the landslide that could not be directly observed from the LOS measures obtained with MSBAS-1D (Fig. 5).

Figs. 5–7 also highlight other ground deformation processes outside of the Funu landslide. At point P2 is observed the deformation associated with another old, deep-seated landslide, as already stressed in Nobile et al., 2018. Deformation observed at the northern limit of the



(a) First derivative along north direction



(b) First derivative along east direction

Fig. 4. Central first derivatives of 1 arc-second (~30 m) resolution SRTM DEM in north direction (a) and in east direction (b) used in the computation of the three-dimensional deformation with MSBAS-3D.

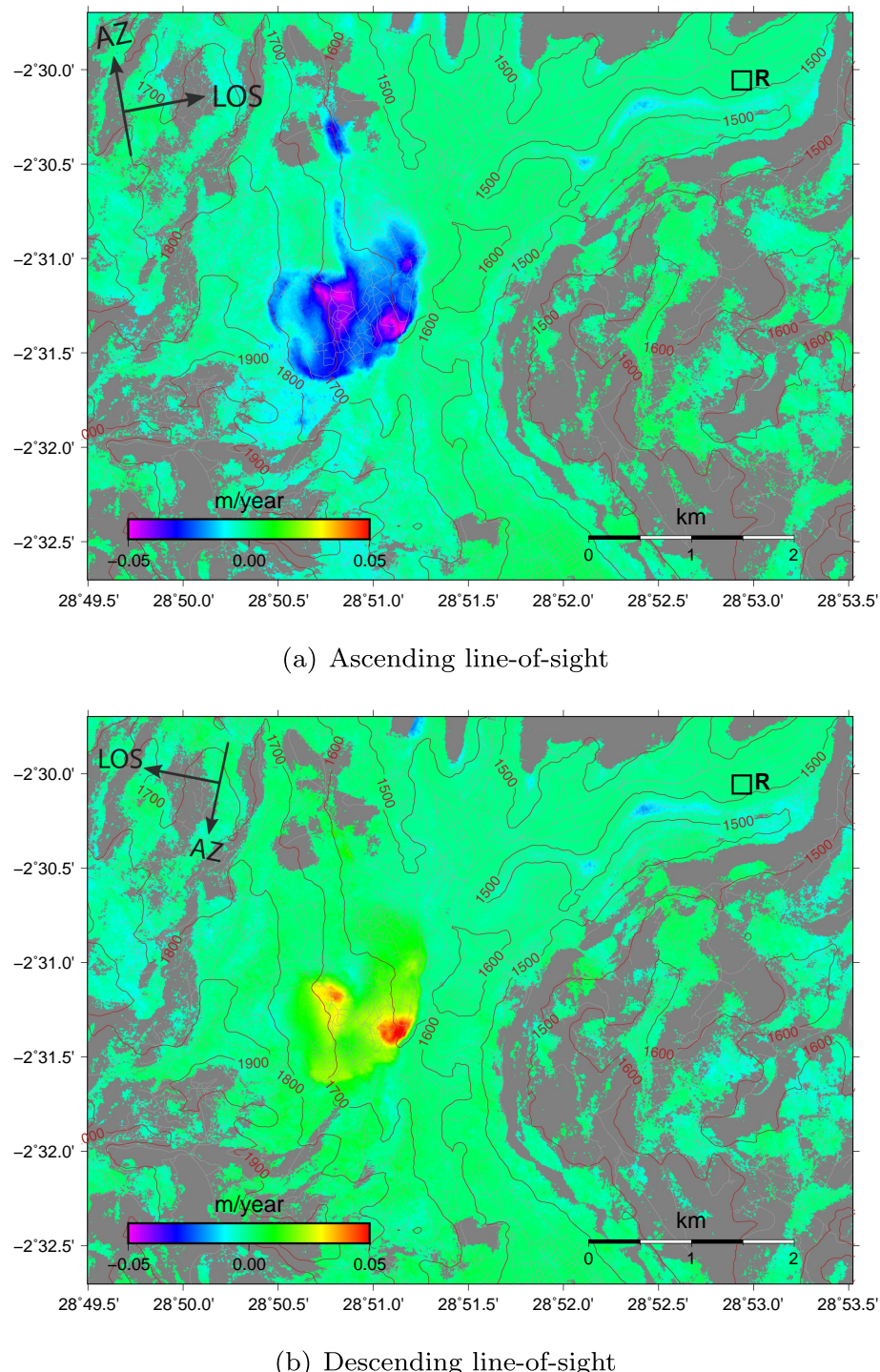


Fig. 5. Maps of linear deformation rate in the radar line-of-sight (LOS) geometry computed using MSBAS-1D from COSMO-SkyMed ascending (a) and descending (b) SAR data. Displacements along LOS direction have to be interpreted as a one-dimensional component of the full 3-D displacement vector. Red colour represents motion towards satellite and blue colour represents motion away from satellite. 100 m elevation contour lines are plotted in brown. Streets are plotted in gray (downloaded from <http://overpass-turbo.eu/>). Average SAR backscatter intensity is exposed in decorrelated areas. (For interpretation of the references to colour in this figure legend, the reader is referred to the web version of this article.)

city is probably associated to subsidence of recently urbanized river delta deposits. As similar origin is inferred for documented subsidence over the flat valley bottom east of the study area (red insert). These patterns of deformation were also observed in the field (Kalikone Buzera et al., 2017). Even though the purpose of our research was not to focus on those areas, this further confirms the reliability of the DInSAR processing.

5. Discussion and conclusions

Working on ascending and descending interferograms computed prior to the MSBAS analysis and geocoded to a common grid, the MSBAS method computed 1D, 2D, and constrained to the parallel surface flow 3D surface deformation time series. From those time series, MSBAS computed map of linear deformation rates for a large, slow-

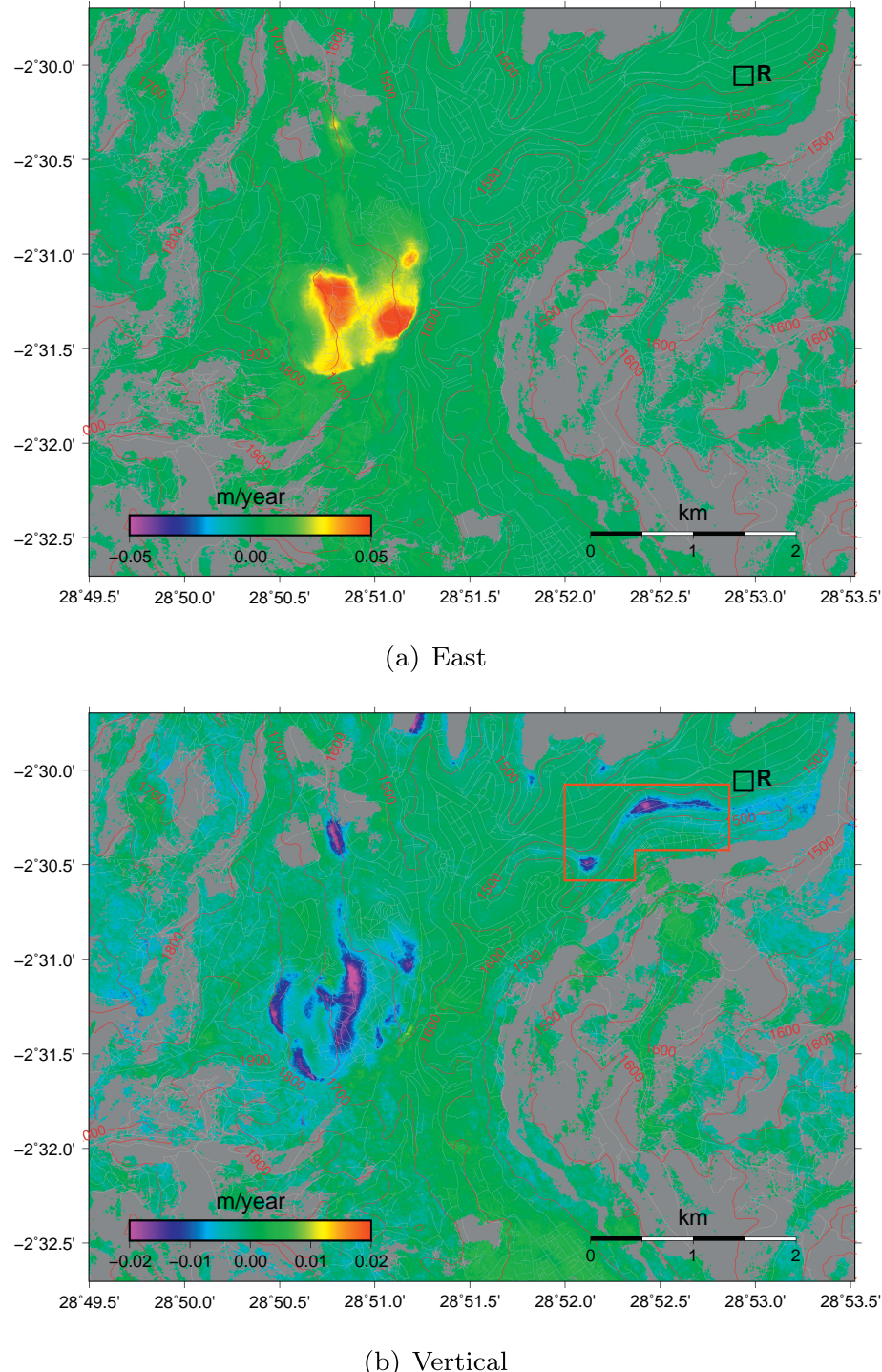


Fig. 6. East (a) and vertical (b) components of linear deformation rate computed using MSBAS-2D from combined COSMO-SkyMed ascending and descending SAR datasets. 100 m elevation contour lines are plotted in brown. R is reference region. Subsiding area that does not deform according to (4) is outlined in red. Streets are plotted in gray (downloaded from <http://overpass-turbo.eu/>). Average SAR backscatter intensity is exposed in decorrelated areas. (For interpretation of the references to colour in this figure legend, the reader is referred to the web version of this article.)

moving, deep-seated landslide in the city of Bukavu. The advantages and disadvantages of each MSBAS and similar methods are summarized in Table 2.

The LOS measures of deformation obtained with the MSBAS-1D

method (Fig. 5) are consistent with the multi-temporal DInSAR SBAS results obtained over a one-year period by Nobile et al., 2018. Overall, the MSBAS results are in agreement with dGNSS measurements with the exception of one zone of the landslide that corresponds to a recent

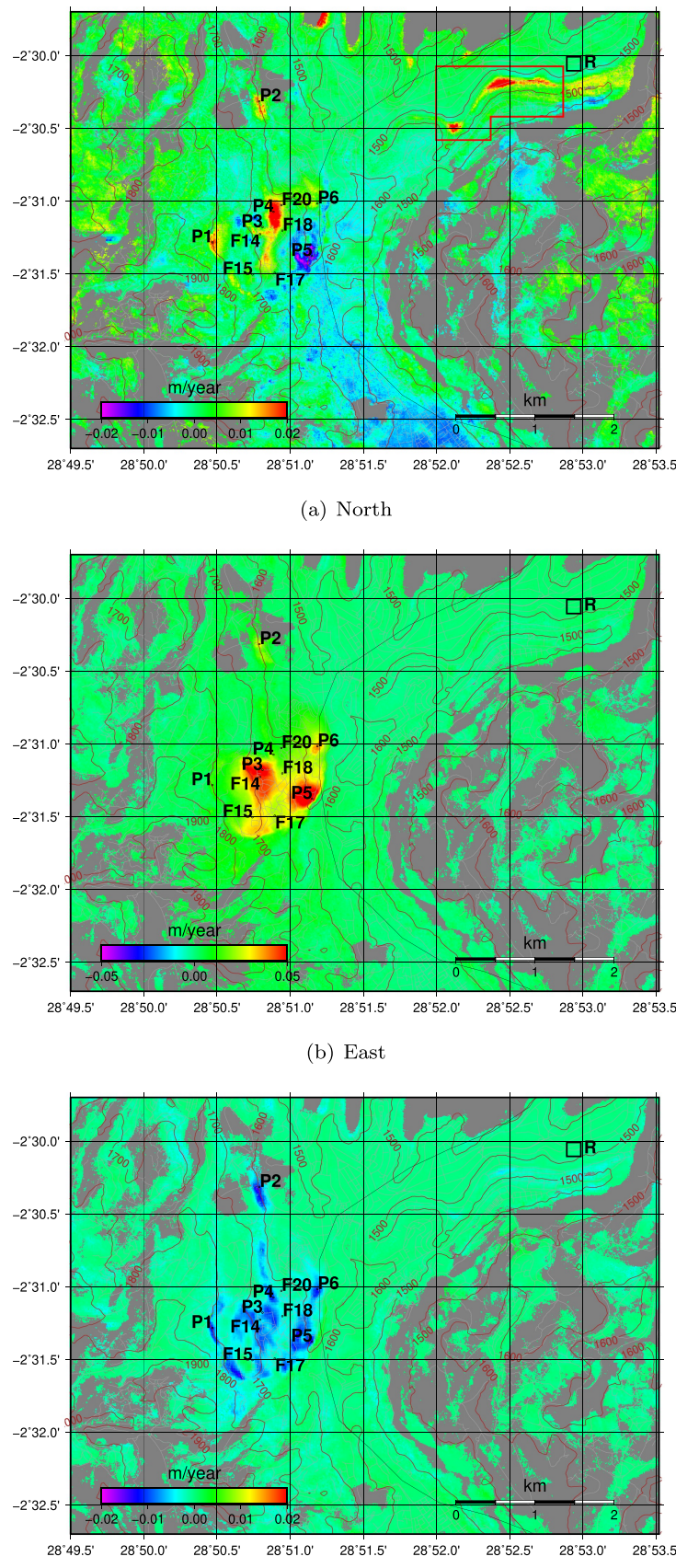


Fig. 7. North (a), east (b), and vertical (c) components of linear deformation rate computed using MSBAS-3D from combined COSMO-SkyMed ascending and descending SAR datasets. 100 m elevation contour lines are plotted in brown. R is reference region. Subsiding area that does not deform according to (4) is outlined in red. Streets are plotted in gray (downloaded from <http://overpass-turbo.eu/>). Average SAR backscatter intensity is exposed in decorrelated areas. Points F14, F15, F17, F18, F20 mark location of campaign GNSS sites. For points P1-P6 that approximately correspond to regions of fastest motion time series are provided in Fig. 9. (For interpretation of the references to colour in this figure legend, the reader is referred to the web version of this article.)

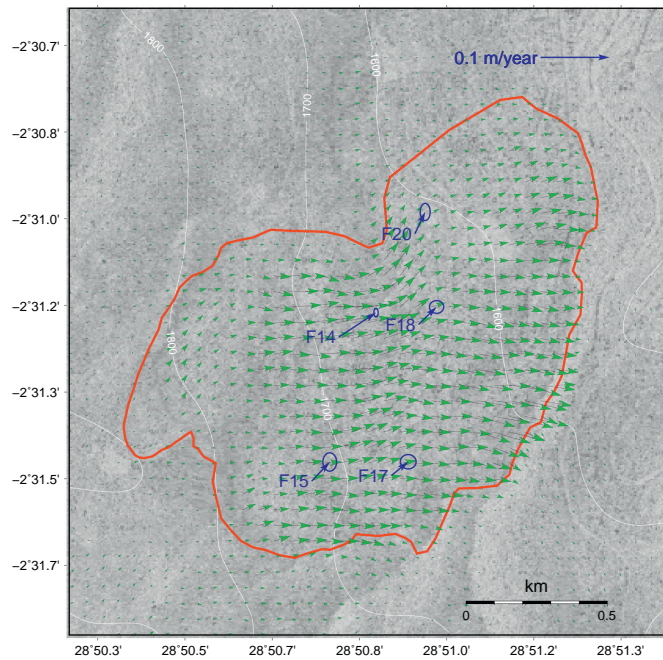


Fig. 8. Horizontal deformation rate vectors computed from COSMO-SkyMed ascending and descending DInSAR data with MSBAS-3D technique are in green. Horizontal deformation vectors with 2σ (i.e. 95%) confidence interval ellipses computed from campaign GNSS data for selected sites F14, F15, F17, F18, F20 are in blue. Funu landslide outline is in red. 100 m elevation contour lines are in white. Background is SAR intensity. (For interpretation of the references to colour in this figure legend, the reader is referred to the web version of this article.)

subsequent landslide within the large landslide (Fig. 2b); here, dGNSS measurements show deformation of up to 500 mm/yr (Nobile et al., 2018). These high deformation rates as well as the sharp velocity contrast with the zone directly surrounding it (with a deformation rate nearly an order of magnitude lower), lead to either a loss of coherence or an underestimation of the deformation during the unwrapping of the interferograms. Those are however associated with the intrinsic limitations of DInSAR technique with respect to measure of rapid displacements. Speckle offset analysis performed with the GAMMA software on selected long-timespan pairs did not detect these large deformation rates neither.

The benefits provided by decomposing the deformation components were illustrated in Figs. 5–8. Compared to MSBAS-2D and 3D, the limitations associated to the traditional 1D LOS analysis (Fig. 5) are clear. While difficult to interpret and communicate to stakeholders unfamiliar with the concept of 1D LOS viewing geometry (Fuhrmann and Garthwaite, 2019), deformation measured on those maps may also lead to misconception about the underlying processes. For instance, individual north, east and vertical deformation components may cancel each other out when the contribution of horizontal components is equal in magnitude but opposite in sign to the contribution of the vertical component. In extreme cases, deformation may appear entirely absent in one (i.e. either ascending or descending) of LOS deformation maps (e.g. Samsonov et al., 2013, 2014). The 2D and 3D results (Figs. 6–8) are much easier to interpret thanks to the direct discrimination between horizontal and vertical deformation components. The information

gathered about the north component provides additional, non-negligible keys for the understanding of processes at work (see Fig. 8). The 3D solution highlights the presence of an active, advancing landslide front, as well effect of lateral constraints from the surrounding non-moving topography. If this behaviour was anticipated from morphometric analysis of high resolution DEMs and the presence of a large bulge at the landslide toe, this pattern of displacement was completely missed by traditional DInSAR measures (Nobile et al. 2018). With the increase of the understanding of the mechanisms of the landslide (interaction with surrounding topography, future evolution and interaction with downslope stream, etc.), such knowledge also bring information on environmental controls, temporally and spatially-variable external forcing conditions and characteristics of future deformation patterns.

In our example, while the magnitude of the horizontal deformation remains similar between MSBAS-2D and MSBAS-3D, the information about the north component provides clear insights for the understanding of the landslide deformation pattern. The decision of whether to use one or the other will depend on the validity of the Surface Parallel Flow constraint (4) and is case-specific. For many gravity-driven processes, such as landslides and glacier flows, making such an assumption of motion parallel to the surface is a valid approximation. However, even when the assumption of motion parallel to the surface is not strictly correct, the approximate 3D analysis may still provide valuable clues for the understanding of the processes at work that may otherwise go undetected. With our example applied on the city of Bukavu, we also show measure of displacement were expected movement clearly not comply with the assumption of motion parallel to the surface. Besides Funu landslide, the study area encompasses for instance a flat valley bottom that corresponds to an old marsh, recently urbanized and that is subjected to subsidence (Nobile et al., 2018). There, MSBAS-3D incorrectly classifies ground movement as horizontal (Fig. 7(a)), while it is perfectly well grasped with MSBAS-2D (Fig. 6(b)).

In comparison to the method used in Notti et al. (2014); Kalia (2018); Hu et al. (2018, 2019) (Table 2), where the LOS velocity is projected along the steepest downslope to obtain estimates of the landslide motion, MSBAS-3D computes a more general solution. It does not require the motion to occur along the steepest downslope, but only parallel to the surface; which allows to capture lateral motion. The drawback of MSBAS-3D approach is that slope-normal displacements are not allowed. The slope-normal displacements can be produced by mass depletion/accumulation, hydrological loading/unloading, and soil swell/shrink. The magnitude of slope-normal displacements of slow-moving landslides, however, is usually smaller than the magnitude of parallel to the surface displacements. In case of large slope-normal displacements, the Hu et al. (2018) methodology may provide more accurate results.

Other methods commonly used to measure azimuthal deformation have other drawbacks (Table 2). Speckle tracking (e.g. Wright et al., 2004; De Michele et al., 2010; Raucoules et al., 2013; Shi et al., 2018) or Multiple Aperture Interferometry (MAI) (e.g. Gourmelen et al., 2011) approaches are for instance best suited for measuring meter-scale deformation (Fuhrmann and Garthwaite, 2019). When the measured deformation is of lower magnitude (e.g., millimetre- to decimetre-scale displacement associated to slow moving landslides (Hung et al., 2014), the north-south displacement component accuracy provided is much lower to what can be reached with conventional DInSAR. Also, the competing techniques presented in the introduction commonly work on individual (or a series of disconnected) interferograms to derive the 3D

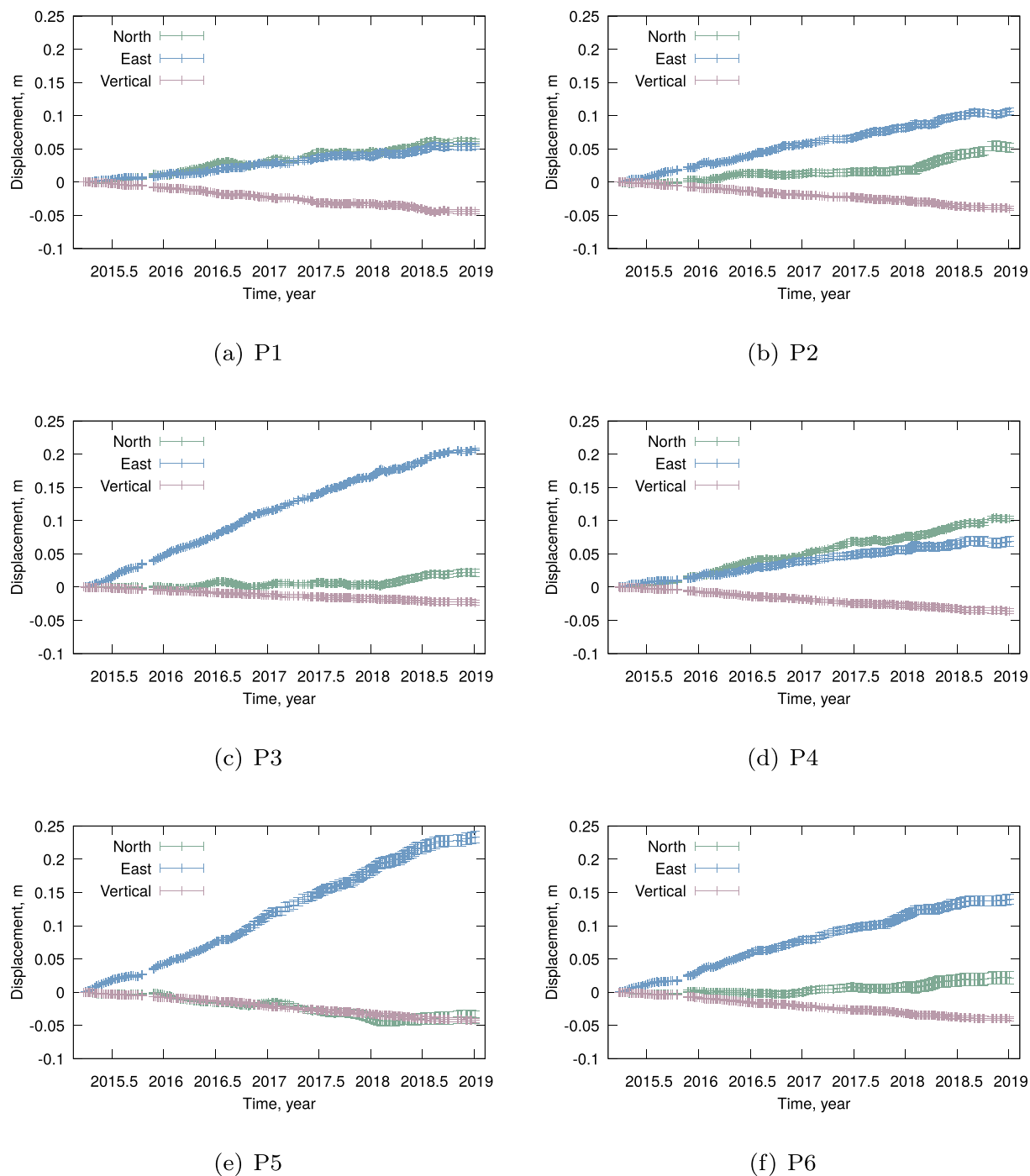


Fig. 9. Three-dimensional time series of ground deformation for points P1-P6 (marked in Fig. 7) that approximately correspond to regions of fastest motion. Standard deviation is computed in 5×5 pixels ($\sim 25 \times 25$ m) window.

deformation. By potentially missing controls of temporally and spatially-variable external forcing on the process kinematic, they are more adapted to the study of sudden deformation events such as earthquakes or volcanic eruptions (Hu et al., 2014). Here lie the strengths of the MSBAS method: producing 3D deformation time series with the accuracy of conventional DInSAR and the spatio-temporal resolution of

modern SAR sensors, it can provide unrivalled insights for studying both long and short-term kinematics of surface processes. Those benefits associated to the 3D decomposition of surface deformation were demonstrated here on a large slow-moving landslide, but this method can be applied to studying many other gravity-driven processes producing motion parallel to the surface.

Table 2

Comparison of methods for resolving deformation components from DInSAR and other SAR-derived data.

	Resolved deformation components	Assumptions and disadvantages
MSBAS-1D	Exact 1D (line-of-sight)	Individual contributions of north, east and vertical deformation components cannot be determined
MSBAS-2D	Approximate 2D (east and vertical)	Negligible north component
MSBAS-3D	Exact 3D	Motion parallel to the surface
De Michele et al. (2010); Gourmelen et al. (2011)	Exact 3D	Requires combination of high (DInSAR) and low (speckle tracking and MAI) precision measurements; can be used for mapping only large deformation
Pepe et al. (2016)	Approximate 3D	Minimum acceleration constraint
Hu et al. (2018)	Exact 3D	Negligible cross-slope component; Motion is allowed in vertical plane in direction of slope aspect

Declaration of Competing Interest

The authors declare that they have no known competing financial interests or personal relationships that could have appeared to influence the work reported in this paper.

Acknowledgments

COSMO-SkyMed images were acquired through RESIST (SR/00/305) and MODUS (SR/00/358) projects (<http://resist.africamuseum.be/>, <http://resist.africamuseum.be/MODUS>) funded by the Belgian Federal Science and Policy Office (BELSPO) and the CEOS Landslide Pilot. The images are under an Italian Space Agency (ASI) licence. Special thanks go to Université Officielle de Bukavu, and particularly to the members of the Department of Geology. They made possible to execute fieldwork in the study area, provided crucial help for the dGNSS acquisition campaigns and useful information on landslide occurrences in the area. We credit OpenStreetMap contributors for providing street data. Figures were plotted with GMT, GDAL and GNUPLOT, and statistical analysis was performed with R software. The work of Antoine Dille was funded by the MODUS SR/00/358 project. The work of Nicolas d'Oreye was funded by the Luxembourg National Research Fund (FNR) under RESIST and SMMIP projects (INTER/STEREOIII/13/05/RESIST/d'Oreye and INTER/MOBILITY/17/11462632/SMMIP/d'Oreye). We deeply thank Elise Monsieurs for her involvement in processing and conducting the dGNSS campaigns.

References

- Balegamire, C., Michellier, C., Berckmans Muhigwa, J., Delvaux, D., Gerard, I., Dewitte, O., 2017. Vulnerability of buildings exposed to landslides: A spatio-temporal assessment in Bukavu (DR Congo). *Geo-Eco-Trop* 41, 263–278.
- Bayer, B., Simoni, A., Schmidt, D., Bertello, L., 2017. Using advanced InSAR techniques to monitor landslide deformations induced by tunneling in the Northern Apennines, Italy. *Eng. Geol.* 226, 20–32.
- Bechor, N., Zebker, H., 2006. Measuring two-dimensional movements using a single InSAR pair. *Geophys. Res. Lett.* 33 (16).
- Berardino, P., Fornaro, G., Lanari, R., 2002. A new algorithm for surface deformation monitoring based on small baseline differential SAR interferograms. *IEEE Trans. Geosci. Remote Sens.* 40 (11), 2375–2383.
- Colesanti, C., Wasowski, J., 2006. Investigating landslides with space-borne Synthetic Aperture Radar (SAR) interferometry. *Eng. Geol.* 88 (3–4), 173–199.
- Costantini, M., 1998. A novel phase unwrapping method based on network programming. *IEEE Trans. Geosci. Remote Sens.* 36 (3), 813–821.
- De Michele, M., Raucooles, D., De Sigoyer, J., Pubellier, M., Chamot-Rooke, N., 2010. Three-dimensional surface displacement of the 2008 May 12 Sichuan earthquake (China) derived from Synthetic Aperture Radar: evidence for rupture on a blind thrust. *Geophys. J. Int.* 183 (3), 1097–1103.
- Delbridge, B.G., Burgmann, R., Fielding, E., Hensley, S., Schulz, W.H., 2016. Three-dimensional surface deformation derived from airborne interferometric UAVSAR: Application to the Slumgullion Landslide. *J. Geophys. Res. Solid Earth* 121 (5), 3951–3977.
- Delvaux, D., Mulumba, J.-L., Ntabwoba Stanislas Sebagenzi, M., Fiama Bondo, S., Kervyn, F., Havenith, H.-B., 2017. Seismic hazard assessment of the Kivu rift segment based on a new seismotectonic zonation model (western branch, East African Rift system). *J. Afr. Earth Sci.* 134, 831–855.
- Depicker, A., Jacobs, L., Delvaux, D., Havenith, H.-B., Maki Mateso, J.-C., Govers, G., Dewitte, O., 2019. The added value of a regional landslide susceptibility assessment: the western branch of the East African Rift. *Geomorphology*, 06886.
- Dewitte, O., Demoulin, A., 2005. Morphometry and kinematics of landslides inferred from precise DTMs in West Belgium. *Nat. Hazards Earth Syst. Sci.* 5, 259–265.
- Dille, A., Kervyn, F., Mugaruka Bibentyo, T., Delvaux, D., Bamulezi Ganza, G., Ilombe Mawe, G., Kalikone Buzera, C., Safari Nakito, E., Moeyersons, J., Monsieurs, E., Nzolang, C., Smets, B., Kervyn, M., Dewitte, O., 2019. Causes and triggers of deep-seated hillslope instability in the tropics - Insights from a 60-year record of Ikoma landslide (DR Congo). *Geomorphology* 345, 106835.
- Dong, J., Liao, M., Xu, Q., Zhang, L., Tang, M., Gong, J., 2018. Detection and displacement characterization of landslides using multi-temporal satellite SAR interferometry: a case study of Danba County in the Dadu River Basin. *Eng. Geol.* 240, 95–109.
- Elliott, J.R., Walters, R.J., Wright, T.J., 2016. The role of space-based observation in understanding and responding to active tectonics and earthquakes. *Nat. Commun.* 7, 13844.
- Fuhrmann, T., Garthwaite, M.C., 2019. Resolving three-dimensional surface motion with InSAR: Constraints from multi-geometry data fusion. *Remote Sens.* 11 (3), 241.
- Goldstein, R., Werner, C., 1998. Radar interferogram filtering for geophysical applications. *Geophys. Res. Lett.* 25 (21), 4035–4038.
- Gourmelen, N., Kim, S.W., Shepherd, A., Park, J.W., Sundal, A.V., Bjrnsson, H., Plisson, F., 2011. Ice velocity determined using conventional and multiple-aperture InSAR. *Earth Planet. Sci. Lett.* 307 (1–2), 156–160.
- Gray, L., 2011. Using multiple RADARSAT InSAR pairs to estimate a full three-dimensional solution for glacial ice movement. *Geophys. Res. Lett.* 38 (L05502).
- Gray, A.L., Short, N., Mattar, K.E., Jezek, K.C., 2001. Velocities and flux of the Filchner Ice Shelf and its tributaries determined from speckle tracking interferometry. *Can. J. Remote. Sens.* 27 (3), 193–206.
- Handwerger, A.L., Fielding, E.J., Huang, M.-H., Bennett, G.L., Liang, C., Schulz, W.H., 2019. Widespread initiation, reactivation, and acceleration of landslides in the Northern California coast ranges due to extreme rainfall. *J. Geophys. Res. Earth Surf.* 124 (7), 1782–1797.
- Hooper, A., 2008. A multi-temporal InSAR method incorporating both persistent scatterer and small baseline approaches. *Geophys. Res. Lett.* 35, 16302.
- Hu, J., Ding, X., Li, Z., Zhu, J., Sun, Q., Zhang, L., 2013. Kalman-filter-based approach for multisensor, multitrack, and multitemporal InSAR. *IEEE Trans. Geosci. Remote Sens.* 51 (7), 4226–4239.
- Hu, J., Li, Z.W., Ding, X.L., Zhu, J.J., Zhang, L., Sun, Q., 2014. Resolving three-dimensional surface displacements from InSAR measurements: A review. *Earth Sci. Rev.* 133, 1–17 ISSN 0012-8252.
- Hu, X., Lu, Z., Pierson, T.C., Kramer, R., George, D.L., 2018. Combining InSAR and GPS to determine transient movement and thickness of a seasonally active low-gradient translational landslide. *Geophys. Res. Lett.* 45 (3), 1453–1462.
- Hu, X., Burgmann, R., Lu, Z., Handwerger, A.L., Wang, T., Miao, R., 2019. Mobility, thickness, and hydraulic diffusivity of the slow-moving Monroe landslide in California revealed by L-band satellite radar interferometry. *J. Geophys. Res. Solid Earth* 124 (7), 7504–7518.
- Hung, O., Leroueil, S., Picarelli, L., Apr 2014. The Varnes classification of landslide types, an update. *Landslides* 11 (2), 167–194.
- Jacobs, L., Dewitte, O., Poesen, J., Delvaux, D., Thiery, W., Kervyn, M., 2016. The Rwenzori Mountains, a landslide-prone region? *Landslides* 13 (3), 519–536.
- Joughin, I.R., Kwok, R., Fahnestock, M.A., 1998. Interferometric estimation of three-dimensional ice-flow using ascending and descending passes. *IEEE Trans. Geosci. Remote Sens.* 36 (1), 25–37.
- Jung, H.-S., Won, J.-S., Kim, S.-W., 2009. An improvement of the performance of Multiple-Aperture SAR Interferometry (MAI). *IEEE Trans. Geosci. Remote Sens.* 47 (8), 2859–2869.
- Kalia, A.C., 2018. Classification of landslide activity on a regional scale using persistent scatterer interferometry at the Moselle Valley (Germany). *Remote Sens.* 10 (12).
- Kalikone Buzera, C., Teganyi, F., Dewitte, O., Michellier, C., 2017. Ground deformation impact on the vulnerability of water and electricity distribution networks in Bukavu (DR Congo). *Geo-Eco-Trop* 41, 279–292.
- Kumar, V., Venkataramana, G., Hgda, K.A., 2011. Glacier surface velocity estimation using SAR interferometry technique applying ascending and descending passes in Himalayas. *Int. J. Appl. Earth Obs. Geoinf.* 13 (4), 545–551.
- Lanari, R., Casu, F., Manzo, M., Zeni, G., Berardino, P., Manunta, M., Pepe, A., 2007. An overview of the small baseline subset algorithm: a DInSAR technique for surface deformation analysis. *Pure Appl. Geophys.* 164 (4), 637–661 ISSN 1420-9136.

- Larsen, I.J., Montgomery, D.R., Korup, O., 2010. Landslide erosion controlled by hillslope material. *Nat. Geosci.* 3, 247–251.
- Leprince, S., Barbot, S., Ayoub, F., Avouac, J., 2007. Automatic and precise orthorectification, coregistration, and subpixel correlation of satellite images, application to ground deformation measurements. *IEEE Trans. Geosci. Remote Sens.* 45 (6), 1529–1558.
- Li, M., Zhang, L., Dong, J., Tang, M., Shi, X., Liao, M., Xu, Q., 2019. Characterization of pre- and post-failure displacements of the huangnibazi landslide in li county with multi-source satellite observations. *Eng. Geol.* 257, 105–140.
- Massonnet, D., Feigl, K., 1998. Radar interferometry and its application to changes in the Earth's surface. *Rev. Geophys.* 36 (4), 441–500.
- Michel, R., Avouac, J.-P., Taboury, J., 1999. Measuring ground displacements from SAR amplitude images: Application to the Landers Earthquake. *Geophys. Res. Lett.* 26 (7), 875–878.
- Michellier, C., Pigeon, P., Kervyn, F., Wolff, E., May 2016. Contextualizing vulnerability assessment: a support to geo-risk management in Central Africa. *Nat. Hazards* 82, 27–42.
- Moeyersons, J., Trfois, P., Lavreau, J., Alimasi, D., Badriyo, I., Mitima, B., Mundala, M., Munganga, D.O., Nahimana, L., 2004. A geomorphological assessment of landslide origin at Bukavu, Democratic Republic of the Congo. *Eng. Geol.* 72 (1–2), 73–87.
- Mohr, J.J., Reeh, N., Madsen, S.N., 1998. Three-dimensional glacial flow and surface elevation measured with radar interferometry. *Nature* 391, 273–276.
- Monsieurs, E., Jacobs, L., Michellier, C., Basimike Tchangaboba, J., Ganza, G.B., Kervyn, F., Maki Mateso, J.-C., Mugaruka Bibentyo, T., Kalikone Buzera, C., Nahimana, L., Ndayisenga, A., Nkurunziza, P., Thiery, W., Demoulin, A., Kervyn, M., Dewitte, O., Nov 2018. Landslide inventory for hazard assessment in a data-poor context: a regional-scale approach in a tropical African environment. *Landslides* 15, 2195–2209.
- Ng, A., Ge, L., Zhang, K., Li, X., 2012. Estimating horizontal and vertical movements due to underground mining using alos palsar. *Eng. Geol.* 143–144, 18–27.
- Nobile, A., Dille, A., Monsieurs, E., Basimike, J., Bibentyo, T.M., d'Oreye, N., Kervyn, F., Dewitte, O., 2018. Multi-temporal dinsar to characterise landslide ground deformations in a tropical urban environment: Focus on Bukavu (DR Congo). *Remote Sens.* 10, 626.
- Notti, D., Herrera, G., Bianchini, S., Meisina, C., Garcia-Davalillo, J.-C., Zucca, F., 2014. A methodology for improving landslide PSI data analysis. *Int. J. Remote Sens.* 35 (6), 2186–2214.
- Pathier, E., Fielding, E.J., Wright, T.J., Walker, R., Parsons, B.E., Hensley, S., 2006. Displacement field and slip distribution of the 2005 Kashmir earthquake from SAR imagery. *Geophys. Res. Lett.* 33 (20).
- Pattyn, F., Derauw, D., 2002. Ice-dynamic conditions of Shirase Glacier, Antarctica, inferred from ERS SAR interferometry. *J. Glaciol.* 48 (163).
- Pepe, A., Calo, F., 2017. A review of interferometric synthetic aperture radar (InSAR) multi-track approaches for the retrieval of earth's surface displacements. *Appl. Sci.* 7 (12).
- Pepe, A., Solaro, G., Calo, F., Dema, C., 2016. A minimum acceleration approach for the retrieval of multiplatform InSAR deformation time series. *IEEE J. Sel. Topics Appl. Earth Observ. Remote Sens.* 9 (8), 3883–3898.
- Raucoules, D., de Michele, M., Malet, J.-P., Ulrich, P., 2013. Time-variable 3D ground displacements from high-resolution synthetic aperture radar (SAR). Application to La Valette landslide (South French Alps). *Remote Sens. Environ.* 139, 198–204.
- Rosen, P., Hensley, P., Joughin, I., Li, F., Madsen, S., Rodriguez, E., Goldstein, R., 2000. Synthetic aperture radar interferometry. *Proc. IEEE* 88 (3), 333–382.
- Samsonov, S., 2010. Topographic correction for ALOS PALSAR interferometry. *IEEE Trans. Geosci. Remote Sens.* 48 (7), 3020–3027.
- Samsonov, S., d'Oreye, N., 2012. Multidimensional time series analysis of ground deformation from multiple InSAR data sets applied to Virunga Volcanic Province. *Geophys. J. Int.* 191 (3), 1095–1108.
- Samsonov, S.V., d'Oreye, N., 2017. Multidimensional Small Baseline Subset (MSBAS) for Two-Dimensional Deformation Analysis: Case Study Mexico City. *Can. J. Remote Sens.* 43.
- Samsonov, S., Tiampo, K., 2006. Analytical optimization of DInSAR and GPS dataset for derivation of three-dimensional surface motion. *Geosci. Remote Sens. Lett.* 3 (1), 107–111.
- Samsonov, S., Tiampo, K., Rundle, J., Li, Z., 2007. Application of DInSAR-GPS optimization for derivation of fine scale surface motion maps of southern California. *IEEE Trans. Geosci. Remote Sens.* 45 (2), 512–521.
- Samsonov, S., Tiampo, K., Rundle, J., 2008. Application of DInSAR-GPS optimization for derivation of three dimensional surface motion of southern California region along the San Andreas fault. *Comput. Geosci.* 34 (5), 503–514.
- Samsonov, S., Gonzalez, P., Tiampo, K., d'Oreye, N., 2013. Methodology for spatio-temporal analysis of ground deformation occurring near Rice Lake (Saskatchewan) observed by RADARSAT-2 DInSAR during 2008–2011. *Can. J. Remote Sens.* 39 (1), 27–33.
- Samsonov, S., Gonzalez, P., Tiampo, K., d'Oreye, N., 2014. Modeling of fast ground subsidence observed in southern Saskatchewan (Canada) during 2008–2011. *Nat. Hazards Earth Sys. Sci.* 14, 247–257.
- Shi, X., Zhang, L., Zhou, C., Li, M., Liao, M., 2018. Retrieval of time series three-dimensional landslide surface displacements from multi-angularSAR observations. *Landslides* 15 (5), 1015–1027.
- Tikhonov, A.N., Arsenin, V.Y., 1977. Solution of Ill-Posed Problems. John Wiley & Sons.
- Usai, S., 2003. A least squares database approach for SAR interferometric data. *IEEE Trans. Geosci. Remote Sens.* 41 (4), 753–760.
- Wasowski, J., Bovenga, F., 2014. Investigating landslides and unstable slopes with satellite Multi Temporal Interferometry: current issues and future perspectives. *Eng. Geol.* 174 (23), 103–138.
- Wegmüller, U., Werner, C., 1997. GAMMA SAR processor and interferometry software. In: The 3rd ERS Symposium on Space at the Service of our Environment. Florence, Italy.
- Wright, T.J., Parsons, B.E., Lu, Z., 2004. Toward mapping surface deformation in three dimensions using InSAR. *Geophys. Res. Lett.* 31, L01607.